PCCP

Direct conversion of carbon nanofibers into diamond nanofibers using nanosecond pulsed laser annealing

Journal:	*Physical Chemistry Chemical Physics*
Manuscript ID	CP-ART-01-2019-000063.R1
Article Type:	Paper
Date Submitted by the Author:	20-Feb-2019
Complete List of Authors:	Bhaumik, Anagh; North Carolina State University, Department of Materials Science and Engineering Narayan, Jagdish; North Carolina State University , Materials Science and Engineering

Direct conversion of carbon nanofibers into diamond nanofibers using nanosecond pulsed laser annealing

Anagh Bhaumik[1], Jagdish Narayan[1*]

[1]Department of Materials Science and Engineering, Centennial Campus

North Carolina State University, Raleigh, NC 27695-7907, USA

*Corresponding author. Tel: 919-515-7874. E-mail: narayan@ncsu.edu (Jagdish Narayan)

Abstract

Here, we show the direct conversion of carbon nanofibers (CNFs) into diamond nanofibers (DNFs) by irradiating CNFs with ArF nanosecond laser at room temperature and atmospheric pressure. The nanosecond laser pulses melt the tip of CNFs into a highly undercooled state, and its subsequent quenching results in the formation of DNFs. This formation of DNFs is dependent on the degree of undercooling which is controlled by nanosecond laser energy density and one-dimensional heat flow characteristics in CNFs. The conversion process starts at the top and it extends with the number of pulses. Therefore, our highly non-equilibrium nanosecond laser processing opens a new frontier for the synthesis of exciting pure and doped diamond structures at ambient temperatures and pressures for a variety of applications.

1. Introduction

The wonders and challenges in carbon have fueled several exciting opportunities and scientific discoveries for more than half a century.[1,2] The conversion of the sixth most abundant element in the Earth's crust, carbon into diamond at room temperatures and atmospheric pressures, has always been a matter of great interest to the carbon scientific community.[3] Many approaches have been undertaken in the past to convert graphite into diamond at high temperatures and pressures (HPHT), plasma enhanced chemical vapor deposition (PECVD), microwave annealing at high temperature and pressure, and in the presence of a catalyst.[4-6] There are reports of diamond formation from carbon nanotubes and fibers at low temperatures and pressures using spark plasma sintering, ballistic fracturing, and chemical processing, which exhibits limited yield and control.[7-12] The conversion of carbon nanotubes and fibers into diamond has been also reported at high temperatures and high pressures *via* the formation of intermediate quasi-spherical onion-like structures.[13-16] Interesting nanostructures of diamond are also formed onto CNTs after hydrogen plasma treatment.[17,18] The formation of nanocrystalline diamonds from CNTs using hydrogen chemisorption is similar to that in chemical vapor deposition (CVD) process, where atomic hydrogen is responsible for creating carbon containing species and formation of diamonds.[19] Similar growth of diamonds (on Si) encapsulated in graphitic shells has been also reported using the post-treatment of (atomic) hydrogen.[7] But there was a relatively low yield (~10%) with little control of the dimensions of the diamond structures formed. Recently, picosecond laser assisted formation of new phases of carbon (T-carbon) nanowires from CNTs was also observed.[20] Since this conversion requires first-order phase transformation, the role of picosecond lasers was not clarified.[20] Previous result on conversion of CNTs to quadrilateral crystals of diamond using continuous wave CO_2 laser show sporadic growth of diamonds in a Fe-C alloy system.[21] Previous

reports (theoretical and experimental) have also indicated the formation of carbon-based materials (mostly sp^2-bonded) by using nanosecond laser pulse melting.[22,23] As a result, a method for direct conversion of carbon nanofibers into diamond at ambient temperatures and atmospheric pressures in air will be a major step forward in this field.

This report presents a novel processing route to facilitate the one-step conversion of carbon nanofibers into diamond nanofibers using nanosecond ArF laser at room temperature and atmospheric pressure without any need for catalysts and atomic hydrogen to stabilize sp^3 diamond bonding. The formation of nanodiamonds is an optimal choice for nanomechanical systems and drug delivery due to its high biocompatibility and ease of functionalization.[24,25] Therefore, controlled conversion of graphitic structures to DNFs is a matter of great scientific interest with a tremendous technological impact. The formation of diamond utilizing a low-thermal budget route will revolutionize its use in electronic, biomedical, and photonic devices.[3] Again, the formation of diamond (large band gap material) on graphite will facilitate better design of field-effect transistors having high mobility (due to one-dimensional structure) and large thermal conductivity.[26] Thermodynamically, the low-energy conversion of graphite into diamond is extremely difficult owing to the high surface energy of diamond, which results in a positive value of the change in Gibbs free energy.[27] In our pulsed laser annealing process, undercooling (non-equilibrium) route is utilized and the conversion (of graphite into diamond) is possible as increasing the degree of undercooling results in high nucleation rates and lowers the Gibbs free energy barrier.[28] The restriction of the heat flow (in one-dimensional amorphous CNFs) causes the formation of DNFs. We report a detailed characterization of DNFs using transmission electron microscopy (TEM), selected area electron diffraction (SAED), electron backscatter diffraction (EBSD), high-

resolution scanning electron microscope (SEM), electron dispersive X-ray spectroscopy (EDX), electron energy-loss spectroscopy (EELS), and Raman spectroscopy.

2. Experimental procedure

The CNFs are synthesized in a tube furnace-CVD chamber thermally baked at 800°C. Highly sensitive mass flow controllers are used to introduce Ar (450 sccm) and H_2 (10 sccm) in the tube furnace prior to the CVD processing. The temperature in the CVD furnace is ramped up to 800°C and thermally soaked for 10 min. At this temperature, 25 sccm of C_2H_4 is introduced in the furnace for 30 minutes. After that, the Ar and H_2 gases are flown in the tube furnace and the flow of C_2H_4 was switched off. The temperature is then ramped down to room temperature for 2 hours. The prepared CNFs are ultrasonicated to remove unwanted metallic impurities. These CNFs are irradiated in air with ArF laser pulses (pulse duration = 20ns, wavelength = 193nm, energy density = 0.6-1.0 Jcm^{-2}). Due to the restriction of heat flow in one-dimensional CNFs, melting of amorphous carbon to a highly undercooled state occurs. The undercooled state is subsequently quenched to form nanostructures of diamond at the CNF tip. With increasing the number of nanosecond laser pulses, the entire fibers are converted into diamond. In the present case, we have performed pulsed laser annealing (melting of CNF into a highly undercooled molten carbon and subsequent quenching the undercooled state). The annealing was performed by using nanosecond laser pulses of ArF excimer laser. The pulsed laser annealing process is carried out in atmospheric pressure and room temperature (in air). No external heat is applied during the conversion. The temperature ~4000 K is attained after laser-material interaction, and this undercooled state results in the formation of diamond upon quenching. In the present case, the restriction of heat flow (1D) in CNF provides enough undercooling to cause the conversion. The energy density (required for melting and subsequent quenching) is calculated with respect to the threshold melting of CNFs,

which is dependent on the thermal properties and heat flow geometry. With the increase in laser energy density (>1.0 J/cm^2), the undercooling decreases and formation of graphite occurs. Therefore, undercooling plays an important role in determining the conversion of CNFs into diamond fibers. It should also be noted that, according to the thermodynamic equilibrium phase diagram, carbon/graphite can be converted into diamond at high temperature (5000 K) and pressure (12 GPa). These pressures and temperatures are somewhat reduced in the presence of catalysts.[29] In the present case no catalysts are used for the conversion of CNF into diamond. The CNFs (before and after PLA processing) are dispersed in ethanol and transferred onto copper TEM grids. To facilitate the bleeding of electronic charges, the sample is sandwiched between two copper grids and then mounted in the TEM sample holder. These structures are characterized by TEM, SAED, EBSD, SEM, and Raman spectroscopy (using 532 nm excitation laser). High-resolution SEM (and EDX) and EBSD measurements are carried out using FEI Verios 460L SEM and FEI Quanta 3D FEG FIB-SEM, respectively. EBSD technique helps for phase identification (by Kikuchi patterns) and the structural morphology is characterized using SEM. JEOL 2000 FX is used for performing the TEM and SAED of the CNFs and DNFs. A 200 kV electron beam from LaB6 source (having lattice resolution of 0.14 nm) is used for the TEM imaging and diffraction purposes. A HORIBA Xplora PLUS confocal Raman microscope having 0.5 μm spatial resolution and 532 nm excitation source is used for determining the Raman active vibrational characteristics (at 300 K) of the CNFs and DNFs. The Raman mappings are performed by using a motorized XY stage installed in the confocal Raman microscope. The XPS instrument having PHOIBOS 150 analyzer is used for the XPS survey and high-resolution scans. The X-ray energy (10-14 kV) is derived from the Al/Mg source and the analyzer has less than 1 eV resolution. The XRD 2θ scans

are performed by using the Rigaku D-MAX/A diffractometer with Cu-Kα radiation (wavelength = 0.154 nm).

3. Results and discussion

3.1. Formation of diamond nanofibers:

Figure 1 depicts the conversion of CNFs to DNFs after the nanosecond pulsed laser annealing with a single laser pulse. Before the PLA processing (figure 1(a)), the CNFs have smooth edges and ends, as CNFs comprise of amorphous graphitic carbon. Upon PLA, there occurs a formation of highly undercooled state of molten carbon at the tip of the fibers (due to the restriction of heat flow in one-dimensional CNFs). The PLA process is completed in less than 200 ns. Therefore, the highly undercooled state of molten carbon is quenched to nucleate nanostructures of diamond at the tip of the CNFs. In the tips and bends of the CNFs, the undercooling is the highest, where nanodiamonds are formed. Figure 1(b) shows the formation of nanostructures of diamond at the tip of the CNFs after the PLA technique. The formation of DNFs starts with nucleation of diamond from the highly undercooled state of molten carbon (formed after PLA). The formation of diamonds occurs by a homogeneous nucleation from the highly undercooled state of carbon. The change in Gibbs free energy (ΔG_T) associated with the formation of DNFs consists of a gain in volume energy (~r^3) at the expense of surface energy (~r^2), where r is the radius of diamond nucleus. The change in free energy can be calculated using the equation: $\Delta G_T = \frac{-4}{3}\pi r^3 \frac{\rho\ \Delta H_m}{M_m\ T_m}\Delta T_u + 4\pi r^2 r_s$, where ρ is the density of diamond, ΔH_m is the latent heat of melting, M_m is the molar mass, and $r_s$is the surface free energy between diamond nuclei and the undercooled state of carbon. The first term in the equation is the volume energy term (gain in free energy for the formation of diamond nucleus from the undercooled state) whereas the second one is the surface energy term.

The degree of undercooling, ΔT_u is equal to $T_m - T_r$, where T_m indicates melting point of graphite (~5000 K) and T_r indicates the nucleation temperature (~4000 K). With an increase in the value of ΔT_u, ΔG_T becomes more negative and a conversion of graphite (CNFs) to diamond (CNRs) is favorable. Again, the critical radius and change in Gibbs free energy (at $\frac{d\Delta G_T}{dr} = 0$) is inversely proportional to ΔT_u and ${\Delta T_u}^2$, respectively. Therefore increasing ΔT_u reduces the critical value of diamond radius and change in Gibbs free energy (ΔG_T^*). The rate of nucleation (I) is given by the equation: $I \sim exp\frac{-\Delta G_T^*}{KT_r}$. Therefore, with a decrease in the value of ΔG_T^*, the rate of nucleation increases thereby facilitating the formation of diamond. This time requirement emphasizes the importance of thermal conductivity of the substrate during rapid pulse laser heating. A rough estimate of r^* for diamond nuclei from equation is ~20 Å, where diamond surface free energy r_s is 0.6 Jm^{-2}, T_m=4000 K, ΔH_m=1.0 eV/atom, ΔT_u=1000 K, and ρ = 3.5 gm/cm^{-3}. This is verified experimentally in figure 4(d) and (e). Some of the nanodiamonds are marked in figure 4(e) and a single nanodiamond is shown in the top right inset of figure 4(e). The value of Gibbs free energy is maximum at the critical radius. Therefore, diamond nuclei having radius greater than 2 nm will be favorable for the further growth of nanodiamonds into microdiamonds. The growth velocity (v) is directly related to the undercooling by the following equation: $v = \frac{D_\propto f}{\lambda f_D}\left(1 - e^{\frac{(T_m - T_u)\Delta S}{kT}}\right)$, where, $D_\propto, f, \lambda, f_D, k, T, T_m, T_u$ and ΔS denote the liquid diffusivity (~10^{-8} m^2/sec in liquid state), fraction of the available sites, atomic jump distance, geometrical factor associated with diffusion, Boltzmann constant, temperature, melting temperature, undercooling temperature, and the change in entropy, respectively. An increase in the value of T_u decreases the value of chemical free energy barrier for graphite to crystalline diamond phase transformation. This also increases the velocity of the melt-front. Therefore, the values of undercooling dictate the conversion of amorphous

graphitic phase into diamond *via* the carbon melt. If the cooling rate is slow (low undercooling and low solidification velocity), crystalline graphite is formed whereas with high cooling rates (large undercooling and large solidification velocity), crystalline diamond is formed.

Therefore, the diamond nucleation from highly super undercooled carbon can occur readily after the PLA technique. Figure 1(c) shows the formation of diamond at the tip of a CNF, whereas the base of the CNF is unaltered. There occurs a decrease in volume (volume of diamond=0.65×volume of graphite) after the formation of diamond from graphite and is evident from figure 1(c). The formation of diamond preferably occurs at the tip and bends of CNFs and is evident from figure 1(d). The bottom right inset in figure 1(d) indicates the formation of diamond at the CNF tip. It is interesting to note that these nanodiamond crystallites are surrounded by high-index planes and are not as faceted with low energy planes, as found typically in CVD ("cauliflower") diamond films. The crystallites with high-index planes have been shown to be catalytically more active than low-index ones. The CNFs with diamond tips provide an ideal structure for efficient field electron emission. Therefore, the synthesized nanostructures of diamond onto CNFs using the PLA technique will have immense application in nanocatalysis and field emitting devices. Figure 1(e) shows the formation of nanostructures of diamond at a fairly uniform area at the CNF tips and bends. As mentioned above, the heat flow is restricted at the CNF tips and bends, which causes the nucleation of diamond (due to the undercooling process). The simulation of laser interaction with materials (SLIM) calculations[30] are shown in figure 1(f). The temperature *vs* time plot indicates the onset of melting (of CNF) at ~20 ns. The melting occurs ~4000 K which is ~1000 K below the melting point of graphite. This provides the undercooling necessary to nucleate diamond. The undercooling in CNF depends on the thermal properties and heat flow geometry. Therefore, highest undercooling occurs at the tip of the CNFs and lowest at

the base. The inset of figure 1(f) illustrates the melt-in and growth regions of the CNF at ~4000 K. The SLIM calculations (for 0.6 J/cm^2 laser energy density) indicate the solidification velocity of ~2 m/sec and growth time of 15 ns. The solidification velocity and growth time dictate the size of the diamonds nucleated from the highly undercooled state of carbon. The high values of solidification velocity also indicate the liquid-phase growth of diamonds from CNFs after nanosecond pulsed laser annealing. Similar values of solidification velocity are also reported in PLA-grown Si (from undercooled melt of Si).[31] Figure 2 indicates high-resolution SEM images of DNFs formed from CNFs after nanosecond pulsed laser annealing with 20 laser pulses. By subsequent laser annealing these diamond regions can be extended to form longer DNFs. The formation of nanostructures of diamond occurs in those CNFs which are aligned perpendicular to the nanosecond laser beam (figure 2(a)). The CNFs which are aligned parallel to the laser beam do not convert into diamond. Figure 2(b) depicts SEM-EDX of the tip of DNF (formed after PLA). The EDX spectrum (figure 2(c)) depicts the presence of only C-Kα_1 peak at 0.277 keV (and no other impurity peaks). This proves that the phase transformation of amorphous CNF into diamond occurs in the absence of a catalyst (at room temperature and atmospheric pressure). Figure 2(d) shows CNF transformation into diamond at the tips and bends after the nanosecond PLA technique (using 20 laser shots). A complete transformation of CNFs into DNFs for smaller diameter CNFs, as compared to larger diameter CNFs after 20 laser shots is seen in figure 2(e). The formation of diamond spreads as the number of laser pulses is increased. The CNFs having diameter less than 50 nm are completely converted into diamond after 20 laser shots. We have also observed the formation of diamonds on the surface of the CNFs having higher diameter (50-150 nm) after irradiation with 20 laser shots. As it is evident from figure 2(f) that there occurs a higher electron

contrast (due to negative electron affinity) in the diamonds formed at the CNF tips than that from the graphitic base.

3.2. Electron backscatter diffraction and transmission electron microscopy:

The electron backscatter diffraction (EBSD) by using field-emission scanning electron microscope is performed to determine the phase (of carbon) at the CNF tip and base after PLA. The EBSD results are shown in figure 3(a)-(n) from the CNF tip, bend, and base showing characteristic Kikuchi diffraction pattern of diamond (in red) and graphite (in green). The 70 degrees tilted SEM micrograph (figure 3(a)) shows the presence of (laser treated) CNFs. The tip shows the formation of diamond at the tip of the CNF whereas the base of CNF shows the presence of graphitic phase. The electron probe size used for EBSD Kikuchi pattern determination is ~10 nm and is ideal for determination of Kikuchi diffraction patterns in CNFs. The three-dimensional orientation of diamond and graphite is shown as an inset of figure 3(b) and (c). The EBSD Kikuchi patterns taken from the tip (figure 3(b)) and base (figure 3(c)) of a CNF and are shown in figure 3(d) and (e), respectively. It should also be noted that, there occurs formation of diamond just below the tip also (figure 3(f) and (g)) up to the point where the undercooling is large enough (to nucleate and grow diamond). The Kikuchi diffractions (of diamond) are shown in figure 3(i) and (j). It can be clearly seen that there is a minimal change in the crystal orientation (and Kikuchi diffraction pattern) of the EBSD spots taken at the tip and below the tip. The highest undercooling occurs at the tip and falls as we move more towards the base (of CNF). Below the diamond there is formation of crystalline graphite (lowest undercooling). The formation of crystalline graphite between diamond and amorphous carbon shows that a low undercooling molten carbon converts into graphite, as shown by Dresselhaus and coworkers.[32] The amorphous nature of CNF is unaltered close to its base. As mentioned above, there also occurs nucleation of diamond at the bend of CNF and is

shown in figure 3(h). The characteristic Kikuchi diffraction pattern of diamond from the CNF bend is shown in figure 3(h). The dynamical simulations of the diamond Kikuchi patterns and the corresponding crystal orientations are shown in figures 3(l-n). The dynamical simulations (by using the Bloch wave approach) of the experimentally acquired Kikuchi patterns reduce the background effect and, therefore, accurate crystal orientations can be calculated. It should be noted that the EBSD technique yields accurate results for smooth samples. In the present case, the EBSD technique was used to identify the phase (diamond and graphite). The details of the crystal orientation are calculated by using high-resolution TEM and FFT analysis.

Figure 4 depicts the TEM and SAED analysis of the CNFs and nanostructures of diamond formed on the tip and bends of the CNFs (after the PLA technique). As it is evident from figure 4(a) that there is nucleation of diamond at the tip and bend (inset of figure 4(a)) of amorphous "solid" CNFs. The formation of diamond at the tip of the CNFs also shows its use as electron field emitters. The amplitude contrast microscopy in TEM reveals that the darker region corresponds to denser diamond structure whereas the lighter contrast denotes amorphous CNFs. Since the degree of undercooling is the highest at the tips (and bends) in CNFs, there is a homogeneous nucleation of nanostructures of diamond (from the undercooled melt of carbon). In the selected area diffraction pattern (figure 4(b)) taken from the nanocrystalline diamond region from different rods (in figure 4(a)), there was no evidence for the formation of amorphous phase. The SAED pattern shows characteristic diffraction pattern (ring-like and speckled) of nanocrystalline diamond showing the distinct diffractions peaks of 111, 200, 220, 311, 222, 004, 331, and 333 planes. The diffraction profile is overlaid on figure 4(b). The presence of (200) and (222) diffraction rings in the SAED do not indicate the FCC diffraction pattern. The presence of (200) and (222) rings is due to the double electron diffraction from (1-11) and (11-1) planes and from (200) and (022)

planes, respectively. It should also be noted that since (200) and (222) diffractions are not allowed in the case of diamond, it is not observed in X-ray diffraction experiments. Figure 4(c) shows the amorphous structure of the CNFs (before PLA). The FFT of the amorphous CNF is also shown in the right lower inset in figure 4(c). The initial formation of nanodiamonds (NDs) after the PLA technique is depicted in figure 4(d). As it is evident that there is formation of NDs closer to the surface on the CNFs than the core (as larger undercooling occurs at the surface than at the core). The FFT analysis of the NDs is shown in the lower left inset of figure 4(d). The diffraction pattern shows the presence of 111 diffraction spots (circled in red), corresponding to diamond. This corresponds to <110> cross-section that has two sets of {111} planes of diamond. An inverse FFT of the diffraction pattern (lower right inset in figure 4(d)) shows the presence of lattice planes separated by 0.207 nm (interplanar spacing of {111} planes in diamond). A dense formation of nanostructures of diamond occurs at the tip and bend of CNFs and is shown in figure 4(e). Figure 4(d) and (e) show diamond nuclei in the range of 2-5 nm. It should be mentioned that the nucleation rate is the highest at the tip of the CNFs (where NDs are formed) and with an increase in growth rates, larger diamonds are formed below the nanodiamonds. The top right inset in figure 4(e) indicates the presence of {111} diamond planes in the nanodiamonds. Interestingly, some of the nanodiamonds are twinned. The left inset of figure 4(e) shows the FFT analysis of a twinned diamond, where multiple diffraction spots are observed. The inverse FFT analysis reveals the presence of twin planes along {111} twin boundary and a <110> twin axis. The details of the nanotwinned diamond structures will be published elsewhere. Below the NDs, single crystalline diamonds having <110> texture is formed (figure 4(f)), which is consistent with <110> texture of silicon formed under rapid unseeded crystallization.[27] Similar <110> textured growth is found in the diamond structures grown using the PLA of CNFs (figure 4(f)). The FFT analysis of the top

and bottom portion of TEM micrograph show the presence of <110> textured diamond, as we can see the presence of 111 and 002 diffraction spots. Previous results also indicate the formation of ~100 nm wide nanocrystalline region in the super undercooled state of Si.[31,33,34] In the nanocrystalline region formation of 10 nm size of nanocrystallites Si occurred from the super undercooled state of Si.[33] The nanocrystallites of Si provided nucleation sites for growth of macrograined polycrystalline Si. The laser parameters and thermal conductivities of the substrate and thin film are the shown to be the crucial parameters for achieving the super undercooling process.[28] Therefore, in the present scenario, the tips and bends of CNF absorbs the laser energy and there occurs high localized temperatures (due to restriction of the heat flow) because of high undercooling. This leads to the nucleation of diamond at the tips (and bends) of CNFs. The conversion of graphitic CNFs into diamonds occur without the intermediate stage of formation of diamond onions.[8,35] For the case of amorphous Si and Ge (having diamond cubic lattice), the undercooled states are found to occur at 336 and 241 K below their respective melting temperatures.[36] One of our previous works on nanosecond laser melting (using XeCl Excimer laser having wavelength=308 nm and laser width=45 ns) of carbon implanted copper indicated the formation of diamond (zone-refined on Cu).[37] Interestingly, it should be noted that the nanosecond laser melting of $^{73}Ge^{+}$ and $^{75}As^{+}$ implanted highly oriented pyrolytic graphite (HOPG) using a ruby laser (energy density=0.6-3.0Jcm^{-2}, wavelength=693nm, pulse duration=30ns) did not form diamond.[32] This is due to the presence of highly (thermally) conducting HOPG layers, which produced little or no undercooling. In the present case, the amorphous graphitic phase (in CNFs) can be melted at a much lower temperature (1000 K less than the melting point of crystalline graphite) using nanosecond pulsed laser to create a highly undercooled state of liquid carbon. Upon subsequent quenching of this undercooled state, diamond nanofibers are nucleated. At these

transition temperatures (~4000 K), Gibbs free energy of undercooled molten carbon equals that of diamond. This undercooling shift graphite/diamond/liquid carbon triple point from 5000 K/12 GPa to 4000 K/atmospheric pressure. Therefore, the creation of this undercooled state is critical for the nucleation of nanodiamonds. Recently, we have also demonstrated the formation of a new phase of carbon (Q-carbon), nano-, micro-, and large-area diamond on sapphire substrates utilizing the phenomena of undercooling, where the formation of dense Q-carbon (having 75-85% sp^3 and rest sp^2) phase occurs at the highest degree of undercooling.[28,38] In the above-mentioned process, amorphous carbon is melted in the super undercooled state (by irradiating with nanosecond ArF pulsed laser), and quenched rapidly to form Q-carbon or diamonds. We have also achieved direct conversion of carbon nanotubes into diamond nanorods by this process which will be reported shortly. Figure 5 depicts TEM image (performed in TEM mode in STEM) and core-loss EELS at 300 K of CNF and diamond formed after the PLA technique. The TEM image clearly shows the formation of crystalline structure of diamond from amorphous CNF after pulsed laser annealing. To prevent the damage of the diamond structure under the intense (concentrated) electron beam, TEM mode in STEM microscope is used, which also has better information limit than the conventional TEM. The inset of figure 5(a) shows atomic columns present in the crystalline diamond lattice (after FFT filtering of the atomically resolved STEM image).

3.3. Electron energy-loss spectroscopy, Raman spectroscopy, X-ray diffraction, and X-ray photoelectron spectroscopy:

The room-temperature core-loss EEL spectra (figure 5(b)) of CNF and diamond (after PLA) reveal sp^3 (σ*) and sp^2 (π*) bonding characteristics. The antibonding electronic states are observed at 285 eV (π*) and 292 eV (σ*). The EEL spectrum of diamond (after PLA) is considerably different from that of CNF (before PLA). The π* peak is sharp in the case of CNF (predominantly sp^2-

bonded structure) whereas the σ* peak is prominent in the case of diamond (as compared to CNF). The characteristic fine post-edge structures (at 297, 305, and 326 eV) are also observed in the case of diamond formed after PLA technique. There also occurs a characteristic drop at 302 eV corresponding to the absolute IInd band gap in diamond. The long-range periodic structure of crystalline diamond gives rise to modulation to the density-of-states, as it is evident from the σ* region in EELS of diamond (after PLA). The EELS therefore univocally prove the formation of diamond crystallites after PLA of CNF. On the other hand, the amorphous nature of CNF is evident from the broadening of the antibonding states associated with the σ* electronic state. In CNF there is a local electronic effect arising due to interaction of similar electronic sp^3 states oriented at different direction (amorphous structure). This is also an indication of a disordered arrangement of the tetrahedrally bonded C atoms (sp^3-bonded C) in CNF (before PLA).

Theoretical and experimental results [39,40] suggest that the local bonding structure of liquid carbon can be varied from a mixture of twofold and threefold coordinated atoms at low density (1.27 gcm^{-3}) to fourfold coordinated atoms at high density (3.02 gcm^{-3}). The fourfold coordinated liquid structure corresponds to liquid carbon structure at high pressures. The structure of molten super undercooled carbon, which is formed after the PLA process, is similar to the structure of liquid carbon at high pressures, where conversion into diamond phase occurs. Raman spectroscopy is a very powerful technique to determine the bonding characteristics in carbon (especially in graphite and diamond). Figure 6 depicts Raman spectroscopy of before and after PLA CNFs. In an area of 2 μm^2, 45 Raman spectra are collected and shown in figure 6. As it is evident from figure 6(a) there are three distinct Raman peaks centered at 1340, 1570, and 2680 cm^{-1} corresponding to D, G, and 2D vibrational modes, respectively. The stretching of C-C bonds in-plane (E_{2g}) in sp^2 graphitic materials gives rise to the G vibrational mode.[8,41] This phonon

vibrational mode is highly sensitive to strain (induced by external forces like PLA). There are other factors affecting the G vibrational mode such as clustering, presence of sp^3-bonded carbon, disorder, *etc*.[42] Though there is a small red-shift (~ 4 cm^{-1}) of the Raman active vibrational mode (G) after PLA of CNFs, there is a considerable increase in the FWHM of the mode from 40 to 53 cm^{-1} (figure 6(b)). This indicates a considerable amount of strain in the CNFs after the PLA process due to the formation of nanodiamonds at the tips and bends. The spectral width (of G peak) is also dependent on the creation of electron-hole pair by phonon excitation process (Kohn anomaly).[41] Therefore, the increase in FWHM of G vibrational mode in the nanocomposite structure of diamond and CNF can also be due to the change in the Fermi energy level (at the interface) and will provide exciting structures for future optoelectronic devices. The radial breathing modes (RBM), characteristic of carbon nanotubes (single and multi-walled),[43] are not present in the Raman spectra of CNFs. There is an insignificant change in spectral width and peak position of the second-order (two-phonon process) vibrational mode (2D) in CNFs before and after PLA. But it should be noted that the intensity of 2D/intensity of G peak is ~50% more in after PLA CNFs as compared to that before PLA CNFs. The most interesting change (after PLA) is in the disorder-induced D band as evident in figures 6(c) and (d). As it is evident that the asymmetricity of the D peak increases after the PLA technique. There is a significant change in the Raman spectra between 1250-1450 cm^{-1} in before and after PLA processed CNFs (shown in figure 6(e)). The Raman peak corresponding to nanodiamonds is observed ~1321 cm^{-1} in the CNF samples after PLA processing. The red-shift of ~11 cm^{-1} (from 1332 cm^{-1} in microdiamonds) and spectral broadening are due to phonon confinement[44] in nanosized diamonds (formed after PLA). Also, there is an increase in the intensity of D/intensity of G peak in the CNFs after the PLA processing due to the increase in disorder (decrease of graphitic crystallite domains). Therefore, Raman studies provide a clear

evidence for conversion of CNFs into nanodiamonds (due to laser-assisted melting and resolidification) after the PLA technique. Figure 7 depicts Raman mapping of CNF before PLA, after 1 laser shot, and after 20 laser shots. The 532 nm laser was focused on a spot on the sample and the sample was moved by using a motorized stage during the acquisitions of spectra. Figure 7(a) shows the Raman spectra acquired from the CNF and the "NO CNF" region. This was done to image both the CNF and without the CNF regions. The D, G, and 2D vibrational modes are present in the CNF region. All the spectral maps are normalized and overlaid in the inset image. The image shows a complete absence of all the modes in the "NO CNF" region. Figure 7(b) shows the Raman spectra acquired from the CNF after 1 laser shot and the unaffected (masked) region. This was done to identify the interface between the "before PLA" and "after PLA" regions (figure 7(c)). The Raman spectra shown in figure 7(b) indicate the formation of diamond (peak ~1320 cm^{-1}). The diamond region (from 1310-1332 cm^{-1}) was mapped and shown in figure 7(c). As it is clearly evident from the Raman map that the diamonds are only formed after the PLA process. Similar Raman acquisitions were performed for the CNFs which were irradiated with 20 laser shots (figure 7(d)). The diamond peak is more distinct in the 20 laser shots sample as compared to 1 laser shot sample. This indicates that more diamond transformation was possible after multiple laser shots. The diamond region was also mapped from the 20 laser shots sample (figure 7(e)), which shows a complete absence of diamonds in the "Before PLA" region. Figure 8 depicts the XPS, XRD, and bonding analysis of CNFs before and after PLA. The XPS survey scan (figure 8(a)) shows C 1s and O 1s peaks centered ~ 285 and ~530 eV, respectively in the CNFs (before PLA). The XPS scan also shows the absence of impurity peaks in the CNFs. The high-resolution XPS scans of C 1s for CNFs before and after PLA are shown in figure 8(b). In addition to the C-OH (285.7 eV), C=O (286.6 eV), and OH-C=O (288.6 eV) peaks there are sp^2 and sp^3 carbon

peaks present at 284.0 and 285.0 eV, respectively. The CNF (before PLA) do not show the sp^3 peak as compared to the 1 and 20 laser shots CNF samples. Therefore, XPS confirms the conversion of CNF into diamond after the PLA. Figure 8(c) depicts the XRD scans for CNF (before PLA) and after 1 and 20 laser shots. The diffraction peaks at 26.0^0 and 43.9^0 correspond to graphite (0002) and diamond (111), respectively. There is a considerable broadening of the graphite diffraction peak after the PLA due to a decrease in the crystallite size of graphite (after PLA). The decrease in the crystallite size of graphite after the PLA is also evident from the Raman spectroscopy where there occurs an increase in the intensity of D/intensity of G vibrational mode (after PLA). There is a significant decrease in the FWHM of the diamond peak in the 20 laser shots sample as compared to the 1 laser shot sample. By using the Scherrer equation the (mean) size of the diamond crystallites are calculated to be 5 and 100 nm in 1 and 20 laser shots sample, respectively. This also indicates an increase in size of the diamond fibers after multiple pulse laser shots. Figure 8(d) indicates the Raman spectroscopy and XPS analysis of the before PLA and after PLA (1, 5, 10, and 20 laser shots) CNFs. The sp^3% calculated by using the high-resolution XPS indicates a gradual increase in the sp^3 content after multiple laser shots. The intensity of diamond/intensity of G vibrational mode calculated from the Raman spectroscopy also increases with multiple laser shots. Interestingly, the intensity of D/intensity of G vibrational mode increases drastically after irradiating the CNF with 1 laser shot. There is a minimal change in the ratio with multiple laser shots. This indicates a decrease in the size of the graphite crystallites after the PLA. But with multiple laser shots there is a minimal change in the graphite crystallite size which also indicates that diamond is formed from the super undercooled state of molten carbon.

4. Summary

We have synthesized diamond nanofibers from carbon nanofibers by using a highly non-equilibrium technique of pulsed laser annealing. Upon irradiating the CNFs with nanosecond ArF laser, the tips and bends of the CNFs are melted in a highly undercooled state. The highly undercooled state of carbon is a metastable phase and nanodiamonds nucleate from this state. The process (rapid melting, solidification, and growth) is completed in less than 200 ns. Our results clearly indicate that diamond can be formed at ambient conditions in air from the super undercooled state of carbon without catalyst and atomic hydrogen (CVD process). The nanosecond laser parameters and heat confinement by the one-dimensional CNFs determine the temperature distribution and undercooling and play a critical role in nucleation and growth of nanodiamonds. The nanosecond laser pulses help us to achieve the undercooled state of carbon and upon subsequent quenching leads to the formation of nanodiamonds from CNFs. The nanosecond laser heating and temperature distributions are confined spatially and temporally. Therefore, the tips (and bends) of CNFs melt whereas the underlying areas are unaffected. By subsequent laser pulses, these diamond regions can be extended to form larger diamond nanofibers and nanorods. The formation of DNFs and their heterostructures will have exciting applications ranging from drug delivery to optoelectronics and field emitters. This discovery of conversion of CNF tips into diamond nanofibers at room temperature and atmospheric pressure will open a new frontier for synthesis and processing of diamond nanostructures for a variety of applications.

Acknowledgments

We are grateful to Fan Family Foundation Distinguished Chair Endowment for Professor J. Narayan, and this research was funded by the National Science Foundation (DMR 1735695). We

are also very pleased to acknowledge technical help and useful discussions with John Prater and Roger Narayan.

REFERENCES:

1 S. Seyock, V. Maybeck, E. Scorsone, L. Rousseau, C. Hébert, G. Lissorgues, P. Bergonzo and A. Offenhäusser, Interfacing neurons on carbon nanotubes covered with diamond, *RSC Adv.*, 2017, **7**, 153–160.

2 J. Narayan and A. Bhaumik, Research Update: Direct conversion of amorphous carbon into diamond at ambient pressures and temperatures in air, *APL Mater.*, 2015, **3**, 100702.

3 F. P. Bundy, H. T. Hall, H. M. Strong and R. H. Wentorf, Man-Made Diamonds, *Nature*, 1955, **176**, 51–55.

4 J. C. Angus and C. C. Hayman, Low-pressure, metastable growth of diamond and 'diamondlike' phases., *Science*, 1988, **241**, 913–21.

5 Y. Li, Y. Qian, H. Liao, Y. Ding, L. Yang, C. Xu, F. Li and G. Zhou, A reduction-pyrolysis-catalysis synthesis of diamond, *Science*, 1998, **281**, 246–7.

6 Y. Meng, C. Yan, J. Lai, S. Krasnicki, H. Shu, T. Yu, Q. Liang, H. Mao and R. J. Hemley, Enhanced optical properties of chemical vapor deposited single crystal diamond by low-pressure/high-temperature annealing., *Proc. Natl. Acad. Sci. U. S. A.*, 2008, **105**, 17620–5.

7 C.-H. Hsu, S. G. Cloutier, S. Palefsky and J. Xu, Synthesis of Diamond Nanowires Using Atmospheric-Pressure Chemical Vapor Deposition, *Nano Lett.*, 2010, **10**, 3272–3276.

8 C. Luo, X. Qi, C. Pan and W. Yang, Diamond synthesis from carbon nanofibers at low temperature and low pressure, *Sci. Rep.*, 2015, **5**, 13879.

9 A. R. Kamali and D. J. Fray, Preparation of nanodiamonds from carbon nanoparticles at atmospheric pressure, *Chem. Commun.*, 2015, **51**, 5594–5597.

10 A. Kumar, P. Ann Lin, A. Xue, B. Hao, Y. Khin Yap and R. M. Sankaran, Formation of nanodiamonds at near-ambient conditions via microplasma dissociation of ethanol vapour, *Nat. Commun.*, 2013, **4**, 2618.

11 S. Ozden, L. D. Machado, C. Tiwary, P. A. S. Autreto, R. Vajtai, E. V. Barrera, D. S. Galvao and P. M. Ajayan, Ballistic Fracturing of Carbon Nanotubes, *ACS Appl. Mater. Interfaces*, 2016, **8**, 24819–24825.

12 F. Inzoli, D. Dellasega, V. Russo, R. Caniello, C. Conti, F. Ghezzi and M. Passoni, Nanocrystalline diamond produced by direct current micro-plasma: Investigation of growth dynamics, *Diam. Relat. Mater.*, 2017, **74**, 212–221.

13 W. K. Wang and L. M. Cao, Transformation of Carbon Nanotubes to Diamond at High Pressure and High Temperature, *Russ. Phys. J.*, 2001, **44**, 178–182.

14 F. Zhang, J. Shen, J. Sun, Y. Q. Zhu, G. Wang and G. McCartney, Conversion of carbon nanotubes to diamond by spark plasma sintering, *Carbon N. Y.*, 2005, **43**, 1254–1258.

15 W. Han, S. Fan, Q. Li and C. L. Zhang, Conversion of Nickel Coated Carbon Nanotubes

to Diamond under High Pressure and High Temperature, *Jpn. J. Appl. Phys.*, 1998, **37**, L1085–L1086.

16 H. Mehedi, E. Gheeraert, G. Ferro and P. Siffert, in *AIP Conference Proceedings*, American Institute of Physics, 2010, vol. 1292, pp. 141–144.

17 L. T. Sun, J. L. Gong, D. Z. Zhu, Z. Y. Zhu and S. X. He, Diamond Nanorods from Carbon Nanotubes, *Adv. Mater.*, 2004, **16**, 1849–1853.

18 L. T. Sun, J. L. Gong, Z. Y. Zhu, D. Z. Zhu, S. X. He, Z. X. Wang, Y. Chen and G. Hu, Nanocrystalline diamond from carbon nanotubes, *Appl. Phys. Lett.*, 2004, **84**, 2901–2903.

19 H. Liu and D. S. Dandy, *Diamond chemical vapor deposition : nucleation and early growth stages*, Noyes Publications, 1995.

20 J. Zhang, R. Wang, X. Zhu, A. Pan, C. Han, X. Li, D. Dan Zhao, C. Ma, W. Wang, H. Su and C. Niu, Pseudo-topotactic conversion of carbon nanotubes to T-carbon nanowires under picosecond laser irradiation in methanol, *Nat. Commun.*, 2017, **8**, 683.

21 B. Wei, J. Zhang, J. Liang, W. Liu, Z. Gao and D. Wu, Carbon nanotubes transfer to diamond by laser irradiation, *J. Mater. Sci. Lett.*, 1997, **16**, 402–403.

22 C. B. Cannella and N. Goldman, Carbyne Fiber Synthesis within Evaporating Metallic Liquid Carbon, *J. Phys. Chem. C*, 2015, **119**, 21605–21611.

23 C. S. Casari, C. S. Giannuzzi and V. Russo, Carbon-atom wires produced by nanosecond pulsed laser deposition in a background gas, *Carbon N. Y.*, 2016, **104**, 190–195.

24 R. Narayan, *Diamond-based materials for biomedical applications*, Woodhead publishing, 2013 .

25 A. E. Mengesha and B.-B. C. Youan, Nanodiamonds for drug delivery systems, *Diamond-Based Mater. Biomed. Appl.*, 2013, 186–205.

26 C. W. Padgett, O. Shenderova and D. W. Brenner, Thermal Conductivity of Diamond Nanorods: Molecular Simulation and Scaling Relations, *Nano Lett.*, 2006, **6** , 827–1831.

27 R. Z. Khaliullin, H. Eshet, T. D. Kühne, J. Behler and M. Parrinello, Nucleation mechanism for the direct graphite-to-diamond phase transition, *Nat. Mater.*, 2011, **10**, 693–697.

28 J. Narayan and A. Bhaumik, Novel phase of carbon, ferromagnetism, and conversion into diamond, *J. Appl. Phys.*, 2015, **118**, 215303.

29 B. K. Agarwala, B. P. Singh and S. K. Singhal, A study of graphite-diamond conversion using nickel, invar and monel as catalyst-solvents, *J. Cryst. Growth*, 1986, **74**, 77–88.

30 R. K. Singh and J. Narayan, A novel method for simulating laser-solid interactions in semiconductors and layered structures, *Mater. Sci. Eng. B*, 1989, **3**, 217–230.

31 J. Narayan and C. W. White, Pulsed laser melting of amorphous silicon layers, *Appl. Phys. Lett.*, 1984, **44**, 35–37.

32 J. Steinbeck, G. Braunstein, M. S. Dresselhaus, T. Venkatesan and D. C. Jacobson, A model for pulsed laser melting of graphite, *J. Appl. Phys.*, 1985, **58**, 4374–4382.

33 J. Narayan, C. W. White, O. W. Holland and M. J. Aziz, Phase transformation and impurity redistribution during pulsed laser irradiation of amorphous silicon layers, *J. Appl.*

Phys., 1984, **56**, 1821.

34 R. F. Wood, D. H. Lowndes and J. Narayan, Bulk nucleation and amorphous phase formation in highly undercooled molten silicon, *Appl. Phys. Lett.*, 1984, **44**, 770.

35 B. Wei, J. Zhang, J. Liang and D. Wu, The mechanism of phase transformation from carbon nanotube to diamond, *Carbon N. Y.*, 1998, **36**, 997–1001.

36 B. G. Bagley and H. S. Chen, in *AIP Conference Proceedings*, AIP, 1979, vol. 50, pp. 97–101.

37 J. Narayan, V. P. Godbole and C. W. White, Laser method for synthesis and processing of continuous diamond films on nondiamond substrates., *Science*, 1991, **252**, 416–8.

38 A. Bhaumik and J. Narayan, Synthesis and Characterization of Quenched and Crystalline Phases: Q-Carbon, Q-BN, Diamond and Phase-Pure c-BN, *JOM*, 2018, **70**, 456–463.

39 S. L. Johnson, P. A. Heimann, A. G. MacPhee, A. M. Lindenberg, O. R. Monteiro, Z. Chang, R. W. Lee and R. W. Falcone, Bonding in Liquid Carbon Studied by Time-Resolved X-Ray Absorption Spectroscopy, *Phys. Rev. Lett.*, 2005, **94**, 057407.

40 C. J. Wu, J. N. Glosli, G. Galli and F. H. Ree, Liquid-Liquid Phase Transition in Elemental Carbon: A First-Principles Investigation, *Phys. Rev. Lett.*, 2002, **89**, 135701.

41 M. S. Dresselhaus, A. Jorio, M. Hofmann, G. Dresselhaus and R. Saito, Perspectives on Carbon Nanotubes and Graphene Raman Spectroscopy, *Nano Lett.*, 2010, **10**, 751–758.

42 A. C. Ferrari and J. Robertson, Interpretation of Raman spectra of disordered and amorphous carbon, *Phys. Rev. B*, 2000, **61**, 14095–14107.

43 X.-W. Lei, Q.-Q. Ni, J.-X. Shi and T. Natsuki, Radial breathing mode of carbon nanotubes subjected to axial pressure, *Nanoscale Res. Lett.*, 2011, **6**, 492.

44 S. Prawer and R. J. Nemanich, Raman spectroscopy of diamond and doped diamond., *Philos. Trans. A. Math. Phys. Eng. Sci.*, 2004, **362**, 2537–65.

FIGURES

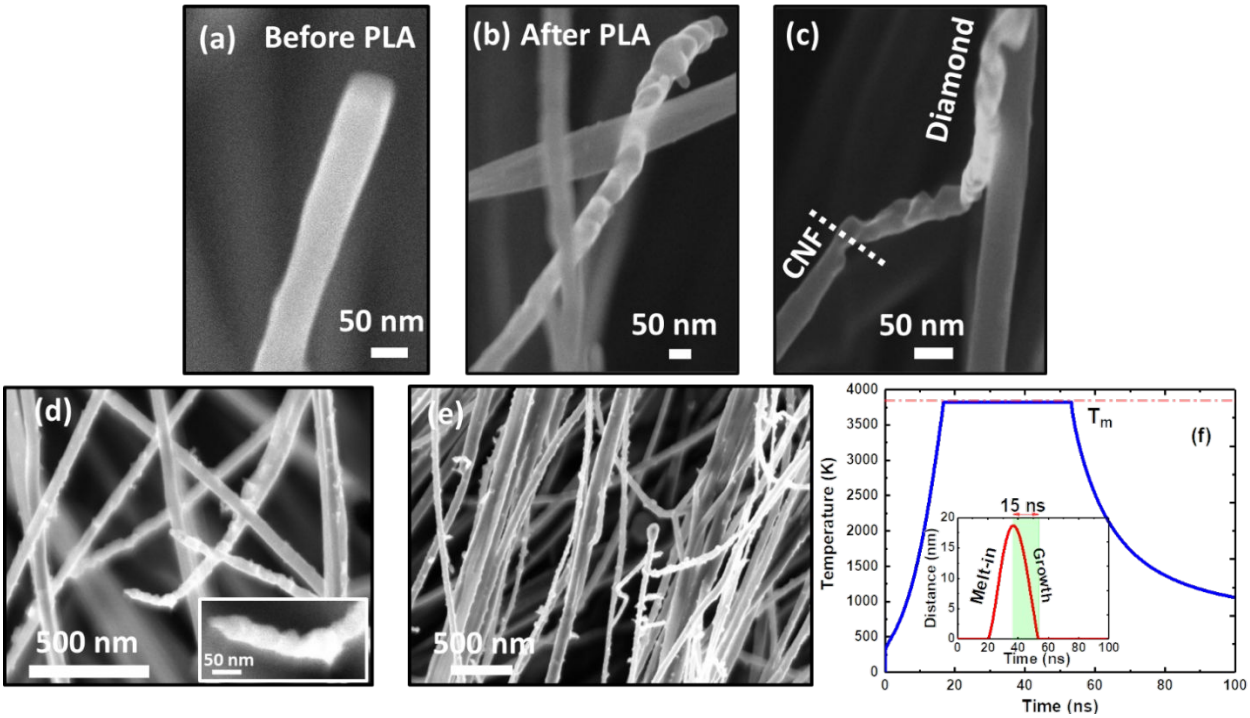

Figure 1: High-resolution SEM images of (a) A CNF before PLA technique, (b) and (c) CNF after PLA showing the formation of nanofibers of diamond at the CNF tip, (d) CNF transformation into diamond at the tips and bends after the nanosecond PLA technique with the inset showing the conversion in one CNF, (e) Phase transformation of CNFs into diamond for smaller diameter CNFs, where one-dimensional heat confinement (high undercooling) occurs at the tips and bends of CNFs, and (f) SLIM calculations of the PLA of CNF with the inset showing the melt-in and growth regions.

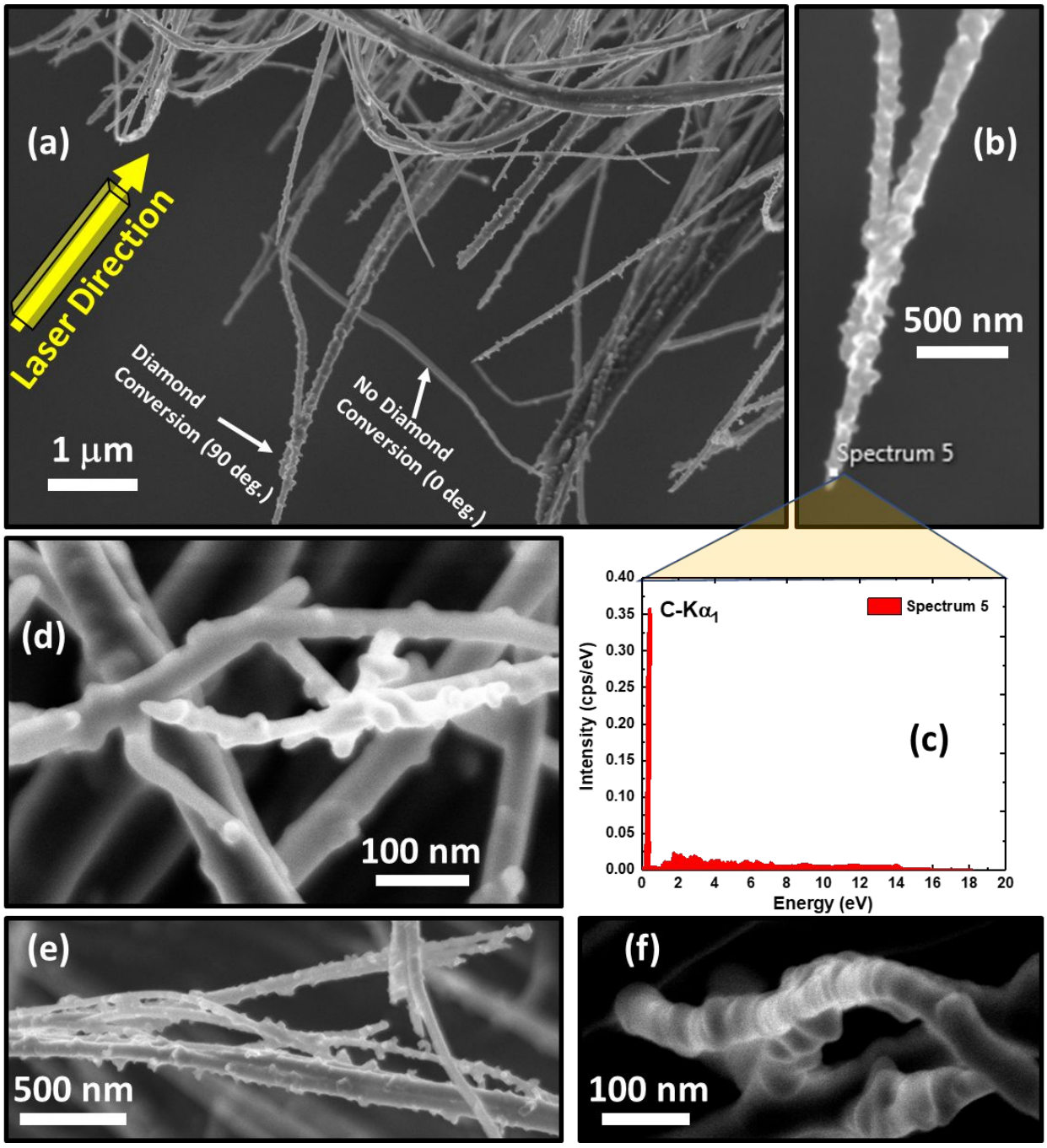

Figure 2: High-resolution SEM images of (a) CNFs after PLA technique (20 laser shots) showing the formation of nanofibers at the CNF tip facing 90 degrees to the nanosecond laser, (b) SEM-EDX of DNFs formed after PLA with the (c) EDX spectra showing the presence of only C-Kα_1 peak at 0.277 keV (and no other impurity peaks), (d) CNF transformation into diamond at the tips and bends after the nanosecond PLA technique (20 laser shots), (e) A complete transformation of CNFs into diamond for smaller diameter CNFs, as compared to larger diameter CNFs after 20 laser shots, and (f) Higher electron contrast (due to negative electron affinity) in the diamonds formed at the CNF tips after the PLA technique.

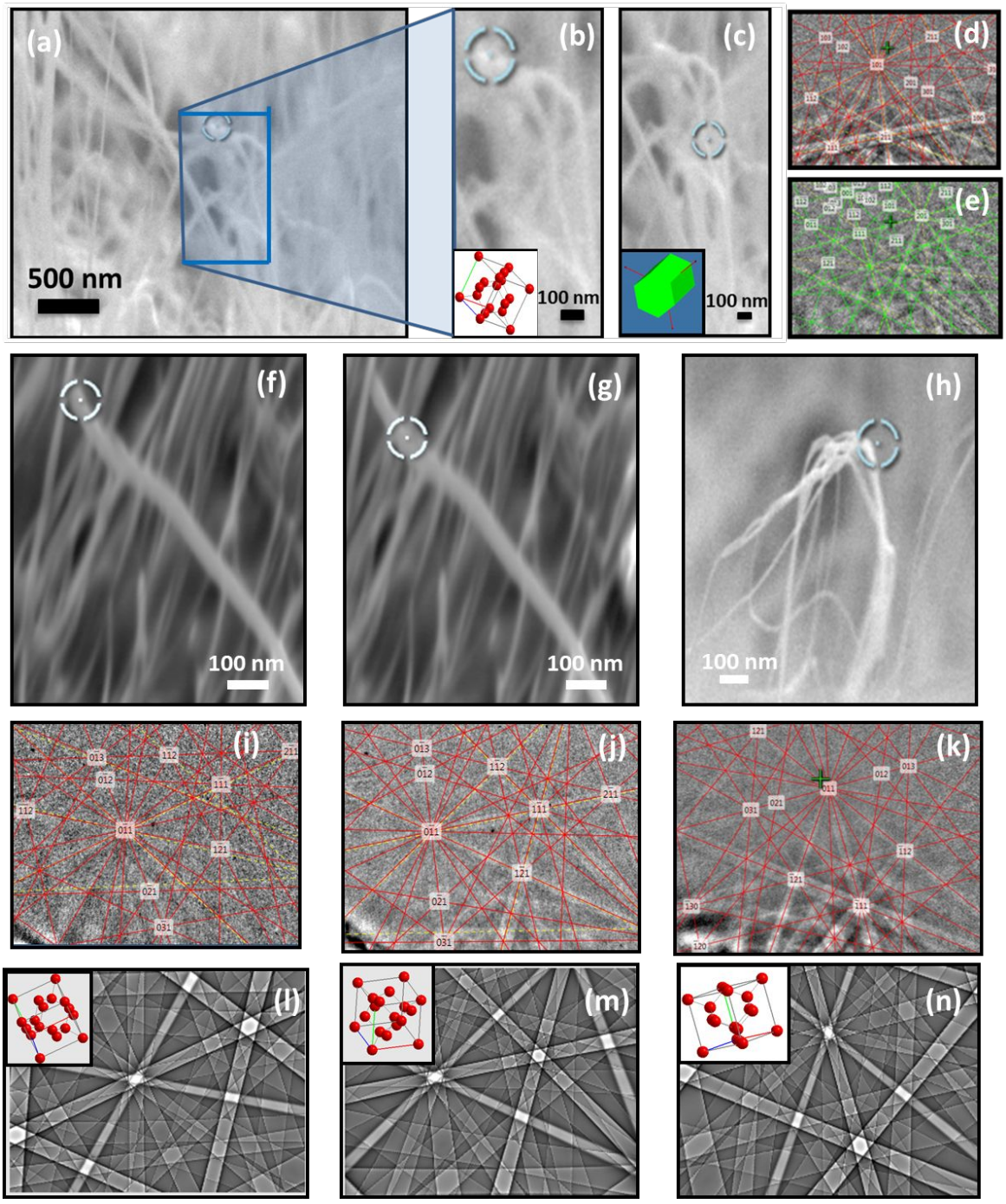

Figure 3: (a) EBSD micrograph showing the formation of diamond at the (b) tip and (c) graphite near the base with the insets showing the three-dimensional crystal orientations, (d) and (e) Kikuchi diffraction patterns of the diamond and graphite, respectively, (f) EBSD micrograph from CNF tip and the corresponding Kikuchi diffraction shown in (i), (g) EBSD micrograph from CNF just below the tip and the corresponding Kikuchi diffraction shown in (j), (h) EBSD micrograph from bend and the corresponding Kikuchi diffraction shown in (k). The dynamical simulations and crystal orientations for the Kikuchi diffractions (i,j,k) are shown in (l,m,n), respectively.

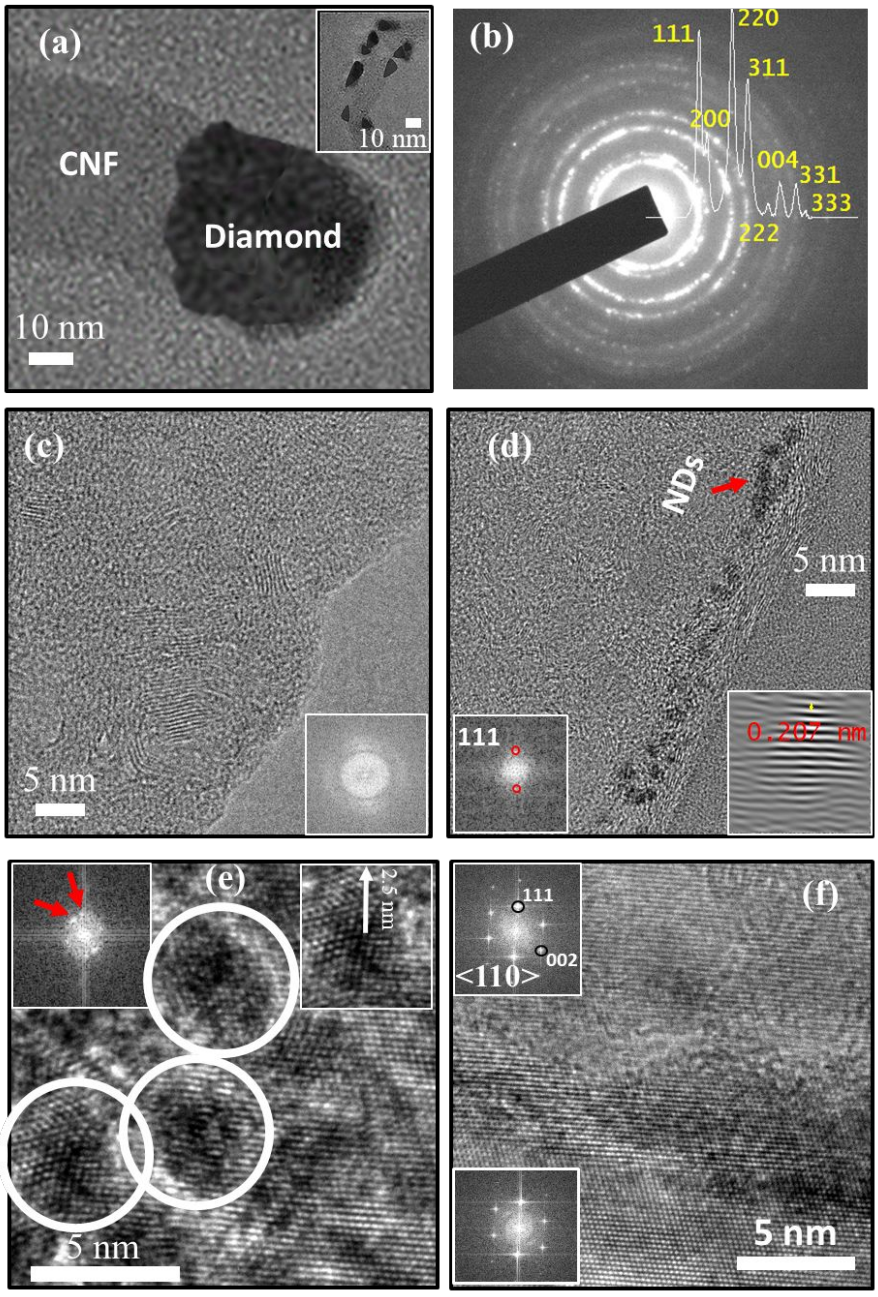

Figure 4: TEM images of (a) formation of diamond at the tip of a CNF after PLA with the inset showing diamond formation at the CNF bend, (b) Selected area electron diffraction pattern of nanodiamonds with the overlaid diffraction spectra showing 111, 200, 220, *etc.* diffraction rings, (c) TEM of CNF before PLA with the inset showing FFT analysis of amorphous CNF, (d) TEM of CNF after PLA showing the nucleation of nanodiamonds at the fiber walls where the undercooling is large with the inset showing FFT analysis showing 111 diffraction spots and the lower right inset showing inverse FFT analysis, (e) TEM image of the nanodiamonds region showing the formation of nanodiamonds (~5 nm) with the top left inset showing the FFT analysis of the nanodiamond showing twin (diffraction) spots, and (f) TEM image of <110> diamonds (inset showing FFT analysis) formed below the nanocrystalline diamond region.

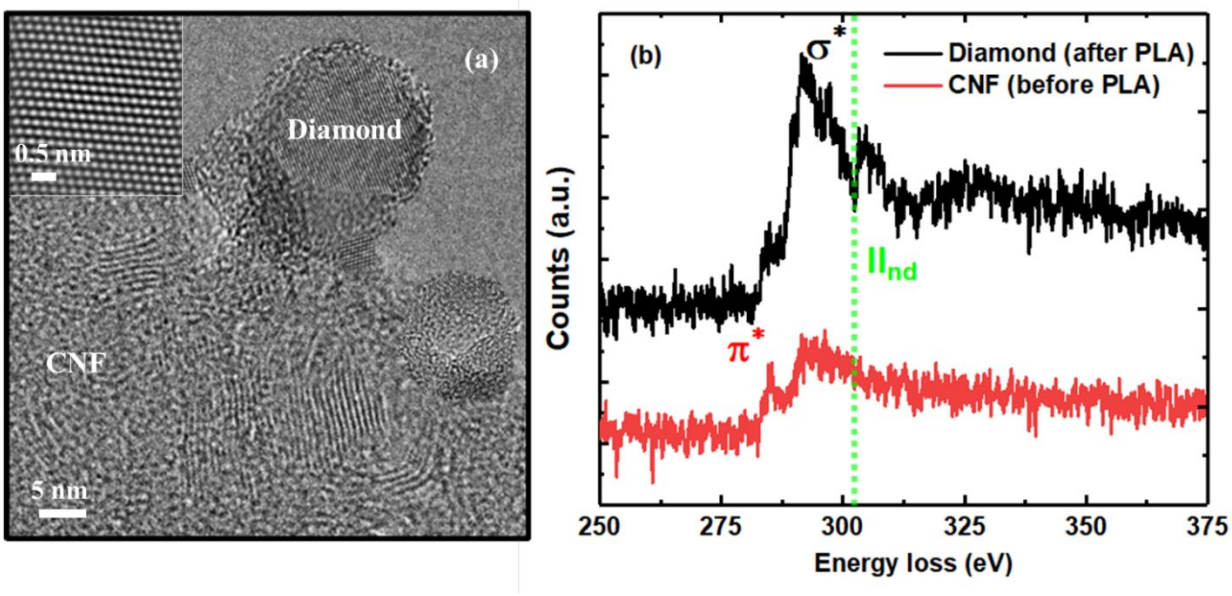

Figure 5: (a) TEM image of formation of diamond from CNF after PLA with the inset showing FFT filtered atomically resolved image of single crystalline diamond (formed after PLA of CNF), and (b) EELS at 300 K of diamond and CNF showing the characteristic π^* and σ^* antibonding electronic states and II_{nd} band gap of diamond.

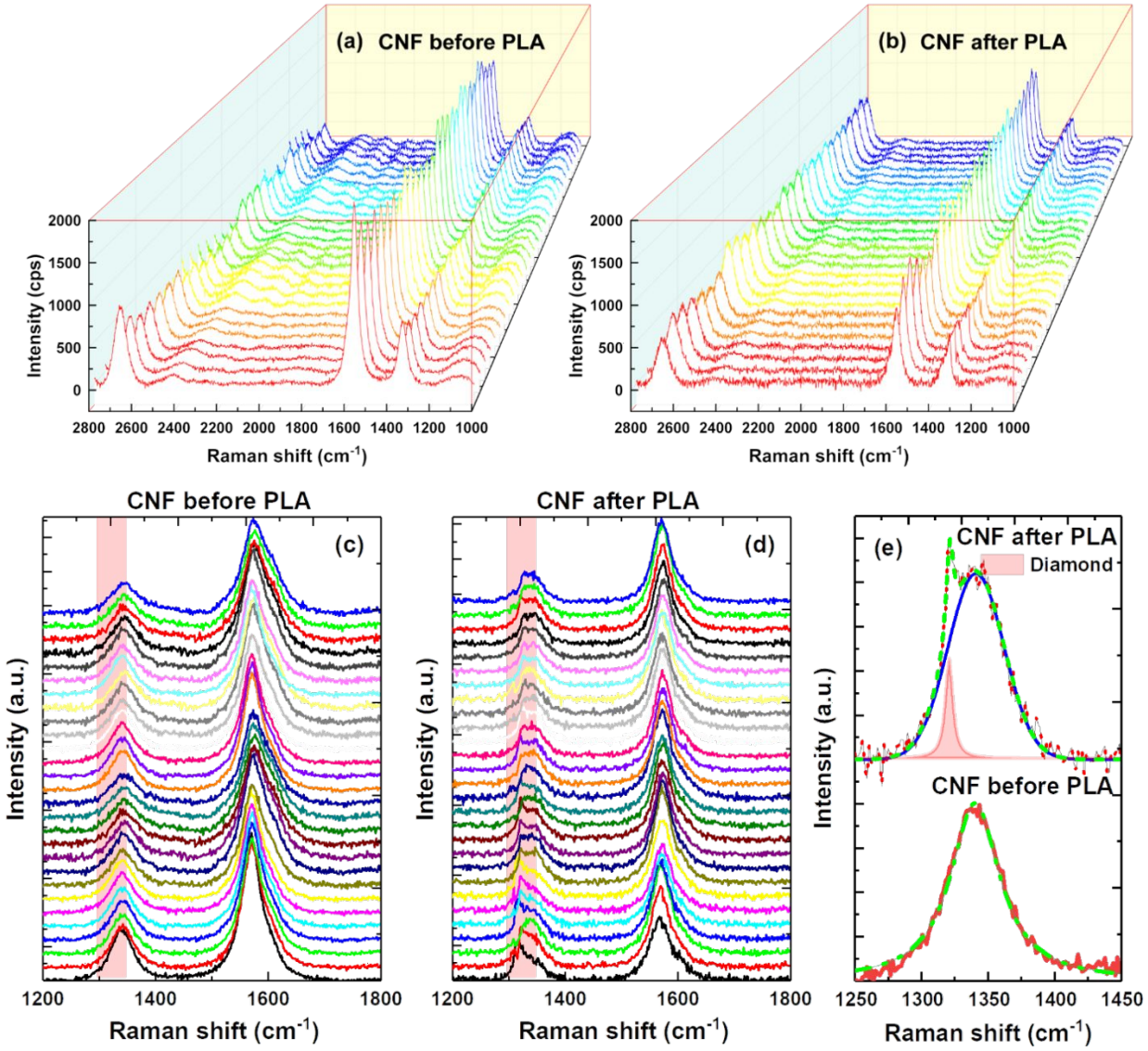

Figure 6: Raman spectroscopy of (a) CNF before PLA, and (b) CNF after PLA in the 1000-2800 cm^{-1} range, (c) CNF before PLA, and (d) CNF after PLA showing D and G vibrational modes (in the range 1200-1800 cm^{-1}) with the red window (having same width) showing the asymmetricity in the D vibrational mode, and (e) showing nanodiamond peak centered at 1321 cm^{-1} in the CNF after PLA.

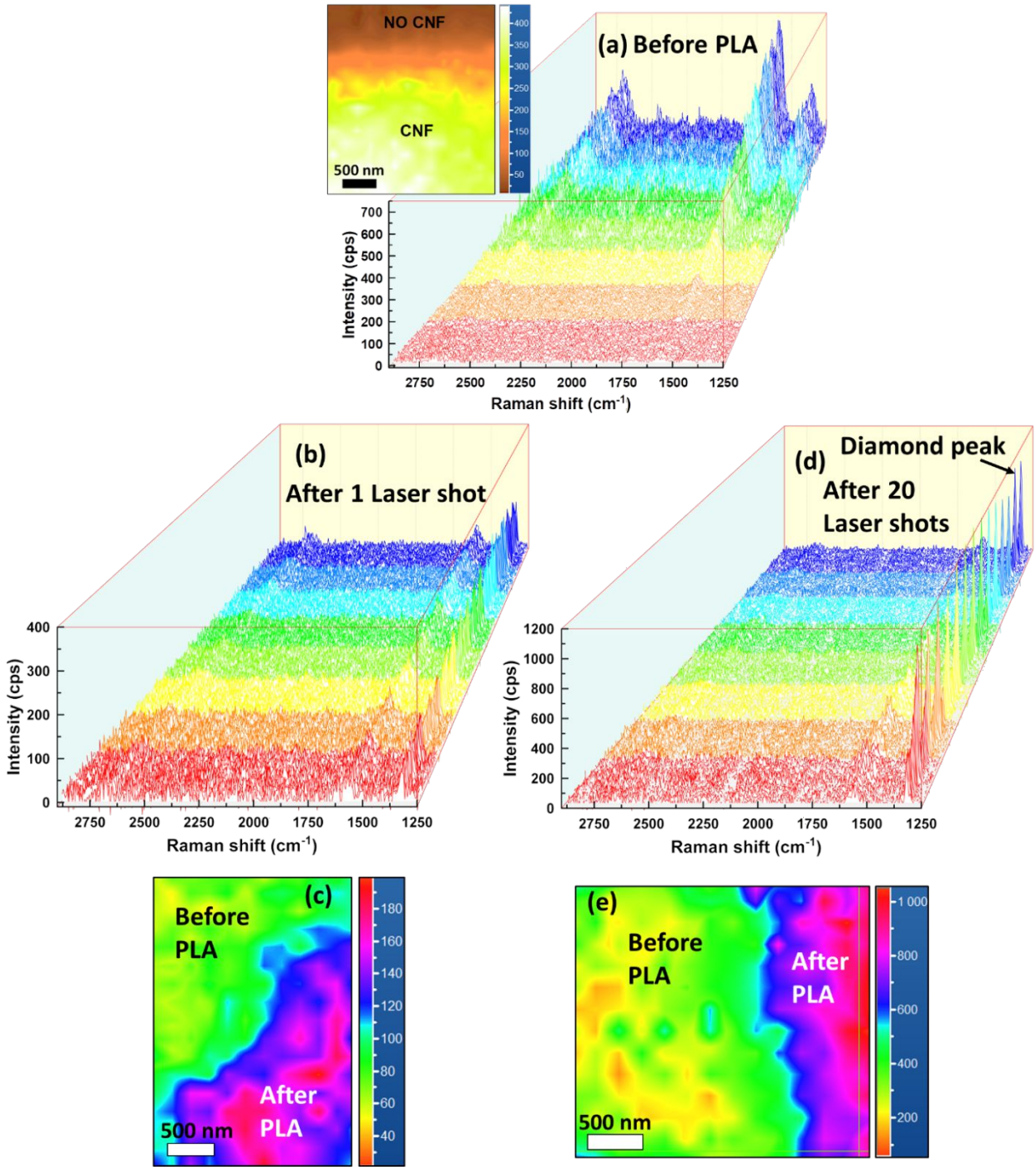

Figure 7: Raman mappings of (a) Before PLA, (b) After 1 laser shot and the corresponding diamond map (spatial distribution) shown in (c), and (d) After 20 laser shots and the corresponding diamond map shown in (e). The diamond map is acquired from the 1310-1332 cm^{-1} region.

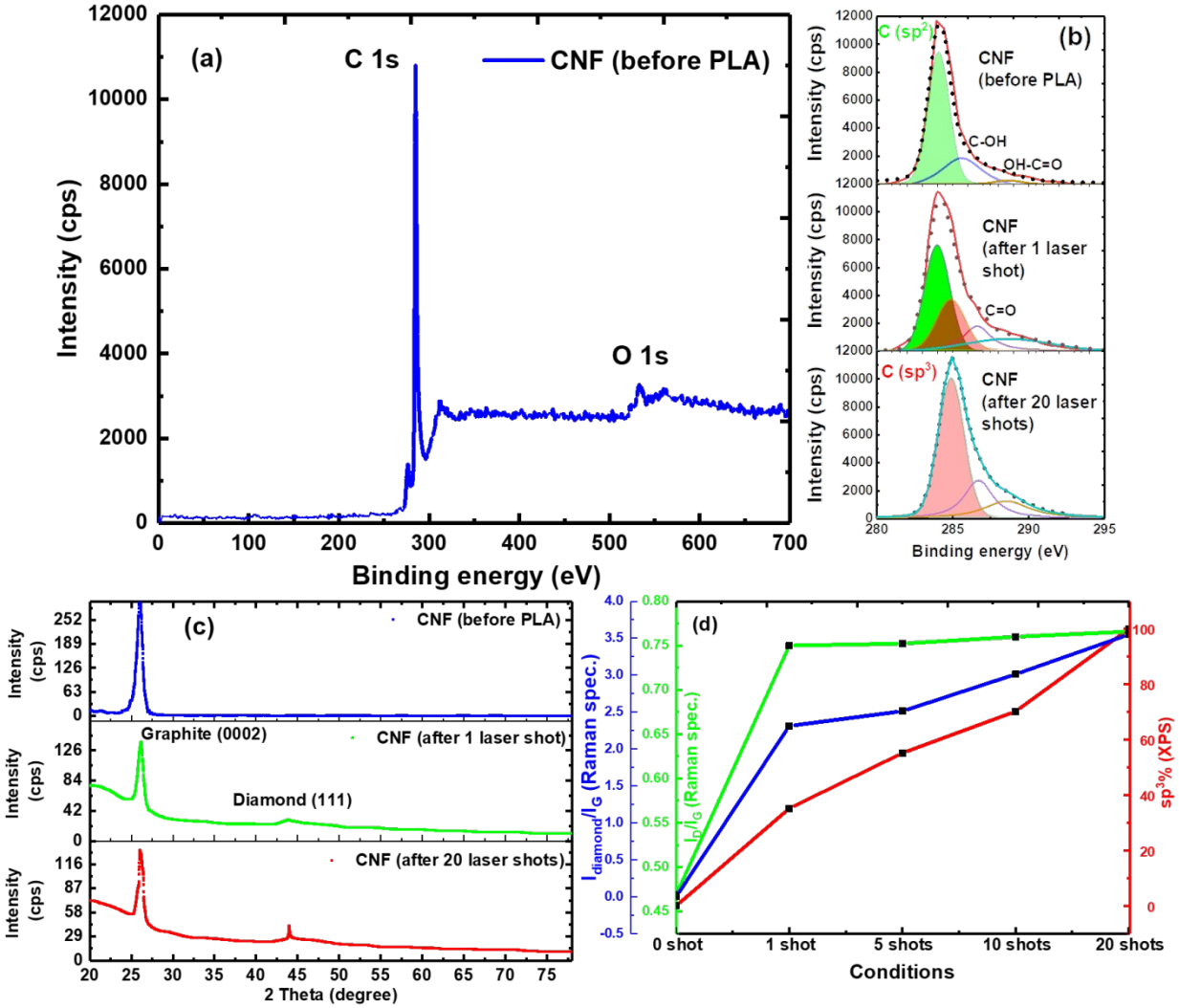

Figure 8: (a) XPS survey scan of the CNF before PLA, (b) High-resolution XPS of the C 1s region for CNF before PLA, after 1 laser shot PLA, and after 20 laser shots, (c) XRD of the CNF before PLA, after 1 laser shot, and 20 laser shots, and (d) Intensity of diamond/intensity of G, intensity of D/intensity of G, and sp^3% (from XPS) *vs* various conditions (0, 1, 5, 10, and 20 laser shots).